LA-UR- LA-UR- 01-1569

Title: WIDE-ANGLE IMAGING LIDAR (WAIL): A GROUND-BASED INSTRUMENT FOR MONITORING THE THICKNESS AND DENSITY OF OPTICALLY THICK CLOUDS

Author(s): Steven P. Love, NIS-2
Anthony B. Davis, NIS-2
Charles A. Rohde, NIS-2
Cheng Ho, NIS-2

Submitted to: SPIE Conference "Laser Radar Technology and Applications VI"
April 16-20, 2001
Orlando, FL

Wide-Angle Imaging Lidar (WAIL): A Ground-Based Instrument for Monitoring the Thickness and Density of Optically Thick Clouds

Steven P. Love,* Anthony B. Davis, Charles A. Rohde, and Cheng Ho
Space & Remote Sensing Sciences Group (NIS-2), Los Alamos National Laboratory

ABSTRACT

Traditional lidar provides little information on dense clouds beyond the range to their base (ceilometry), due to their extreme opacity. At most optical wavelengths, however, laser photons are not absorbed but merely scattered out of the beam, and thus eventually escape the cloud via multiple scattering, producing distinctive extended space- and time-dependent patterns which are, in essence, the cloud's radiative Green functions. These Green functions, essentially "movies" of the time evolution of the spatial distribution of escaping light, are the primary data products of a new type of lidar: Wide Angle Imaging Lidar (WAIL). WAIL data can be used to infer both optical depth and physical thickness of clouds, and hence the cloud liquid water content. The instrumental challenge is to accommodate a radiance field varying over many orders of magnitude and changing over widely varying time-scales. Our implementation uses a high-speed microchannel plate/crossed delay line imaging detector system with a 60-degree full-angle field of view, and a 532 nm doubled Nd:YAG laser. Nighttime field experiments testing various solutions to this problem show excellent agreement with diffusion theory, and retrievals yield plausible values for the optical and geometrical parameters of the observed cloud decks.

1. INTRODUCTION

The interaction of solar radiation with clouds is a pivotal problem in climate research. Clouds play a key role in the atmospheric energy budget, strongly influencing the distribution of energy deposition in the atmosphere, both radiative and convective energy transfer, and the resulting atmospheric dynamics. In the solar (UV-Visible-Near IR, or "shortwave") region, clouds reflect light to space, exerting a cooling effect at lower altitudes, and conversely, by scattering light, increase photon path lengths in the atmosphere, thus enhancing absorption and atmospheric heating; together with thermal IR opacity, these competing effects can lead to either net heating or net cooling on the ground, and help define the temperature distribution throughout the atmosphere. Quantifying the complex interplay of these effects for the many types of real clouds remains one of the greatest problems of climate modeling.

One example of the poor state of understanding of radiation in clouds, and one of the initial motivations for the present work, is the apparent "excess" shortwave absorption suggested by several studies, in which a cloudy atmosphere appears to absorb as much as 25 W/m^2 more solar radiation than can be accounted for by standard models. (To appreciate the magnitude of the problem, note that the IR radiative effect of doubling atmospheric CO_2 is only about 4 W/m^2.) First noted in work comparing passive satellite and ground measurements of shortwave fluxes,[1] the unexplained discrepancy was also seen in multi-aircraft radiometry experiments,[2] and is supported by energy budget considerations in the tropical warm-pool region.[3] If this effect is indeed real, it would have drastic implications for atmospheric dynamics in climate models.[4] Since a photon's probability of absorption by atmospheric gases depends directly on the path length it traverses, a substantial part of the discrepancy between theory and experiment likely lies in the models' oversimplified treatment of multiple scattering. Real clouds, of course, are far from homogeneous. Large 3-D spatial variations occur over length scales from meters to kilometers, and the effect of these variations on multiple scattering is poorly understood, in part because the variations themselves are extremely difficult to quantify in the necessary detail. What is needed is a way of quantifying the multiply scattered pathlengths for the various types of real clouds, and to incorporate these parameterizations into climate models. Experimental mapping of cloud spatial structure in sufficient detail to provide meaningful input to ostensibly more 'realistic' models would be, at best, extremely difficult and time consuming. Fortunately, the quantity of interest for understanding radiation in clouds is not the spatial structure itself, but the distribution of multiply-scattered photon paths which result from it. Direct, actively probed measurement of these distributions for various types of clouds is one of the goals of this work. In addition, other radiatively and meteorologically important cloud parameters , such as vertical thickness and density, and hence liquid water content, can be probed using the new technology, Wide Angle Imaging Lidar (WAIL) described here.

* splove@lanl.gov; phone 505-667-0067; fax 505-667-3815; http://nis-www.lanl.gov/~love ; Space and Remote Sensing Sciences Group (NIS-2), Mail Stop C323, Los Alamos National Laboratory, Los Alamos, NM 87545, USA.

For remote sensing of cloud properties, traditional "on-beam" lidar, which collects returns from only a very narrow field of view (FOV) centered on the transmitted laser beam, yields only a small fraction of the information potentially available and, for the optically thick clouds typical of the boundary layer, is limited to providing the range to the first interface: ceilometry from ground; cloud-top geometry from airborne platforms. With some extra effort, information about the water phase in the first layers can also be inferred by using depolarization[5] and/or multiple-FOV measurements.[6] The key to our work, however, it the recognition that at most visible and near-IR wavelengths lidar photons are not absorbed but merely scattered out of the beam. Much additional information exists in this light exiting the cloud far from the input beam. Since a pulsed laser is essentially a Dirac δ-function in space and time, by measuring the complete spatial and temporal profiles of the returning light one is in effect measuring the Green functions (GFs) of the cloud.

The temporal Green function is, in essence, the distribution of photon path lengths, a quantity which is of interest in itself, as discussed above. In addition, Davis et al.[7,8] showed that other cloud parameters of equal importance can be extracted from off-beam lidar data. The extent of the temporal Green function (i.e., its decay time) is dominated by the physical thickness of the cloud, while the lateral extension of spatial Green function (i.e., its root-mean-square diameter) is influenced strongly by cloud optical depth. These two cloud properties are of direct interest in a variety of meteorological applications, most notably to reduce uncertainties in radiation energetics for climate modeling. They can thus be retrieved from "off-beam" lidar returns, and we demonstrate how further on. As a corollary, one can remotely determine a volume-averaged liquid water content (LWC) via the mean extinction coefficient, i.e., optical depth divided by cloud thickness, and an educated guess at the effective radius. Due to their extreme opacity, the only way to obtain these properties for dense boundary-layer clouds using a conventional lidar is to over-fly and under-fly the layer using an airborne system.[9]

We report here on the status of the emerging technology of WAIL, as implemented for ground-based observations, and the associated retrieval schemes. While we concentrate here on ground-based measurements, we note that one space-based lidar, the Lidar-In-space Technology Experiment (LITE), in spite of having a standard narrow FOV (~3.5 mrad), is effectively an off-beam system due to the large (260 km) range of the target, which leads to a 0.91 km detector FOV at the cloud. A complementary account of cloud-property retrievals based on lidar data collected in space during LITE was given by Davis et al.[10]

The paper is organized as follows. In the next section, we survey the basic theory of off-beam cloud lidar. Section 3 describes the Wide-Angle Imaging Lidar (WAIL) system prototype assembled at LANL. In Section 4, we present field data from this instrument and use it to infer cloud properties. In Section 5, we summarize our findings and outline future work.

2. OFF-BEAM CLOUD LIDAR THEORY

2.1. Definitions

The schematic in Fig. 1 describes the geometry of off-beam cloud lidar observations. The key quantities are cloud optical depth (τ), physical thickness (H), asymmetry factor of scattering phase function (g), and range (d_{obs}). We are interested exclusively in the remotely observable radiative transfer GF ($_{\mathrm{obs}}$), that is, for escaping radiation, excited by a δ-source at the cloud boundary. It will depend parametrically on all of the above cloud quantities as well as two independent variables for space and one for time. The spatial variables can be expressed as Cartesian coordinates (x,y), cylindrical coordinates (ρ,φ), or polar angles (θ_ρ,φ). The temporal variable can be either time elapsed since the pulse impacted the cloud (t), or the "in-cloud" pathlength ($\lambda = ct$), noting that the "out-of-cloud" portion of total pathlength is simply $d_{\mathrm{obs}}(1+1/\cos\theta_\rho)$.

Photon-escape GFs have straightforward interpretations in terms of probability of a photon to escape from the cloud into any direction at position (x,y) and time t, conditional to be either reflected or transmitted: e.g.,

$$G_{\mathrm{R}}(t,x,y)\mathrm{d}x\mathrm{d}y\mathrm{d}t \,/\, R = \mathrm{Prob}\{\text{ escape during } [t,t+\mathrm{d}t),\ \text{from } [x,x+\mathrm{d}x)\otimes[y,y+\mathrm{d}y) \text{ in reflection }\}, \quad (1)$$

where the normalization constant,

$$R = \iiint G_{\mathrm{R}}(t,x,y)\mathrm{d}x\mathrm{d}y\mathrm{d}t, \quad (2)$$

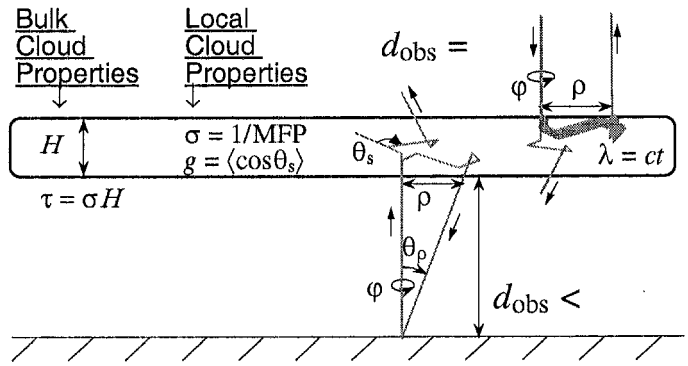

Figure 1: Geometry of Off-Beam Cloud Lidar. From left to right, illustrated meanings for: (1) cloud optical depth τ, physical thickness H, their ratio (extinction σ), and asymmetry factor g (mean cosine of scattering angle ≈ 0.85 for typical droplet populations); (2) independent variables angle (space) θ_ρ and time t, radiance $G_{obs}(\tau,g,H,d_{obs};t,\theta_\rho,\varphi)$ for a ground-based WAIL system and a cloud at finite range d_{obs}; (3) similarly, $G_{obs}(\tau,g,H,\infty;t,\rho,\varphi)$ is measured during a LITE-like mission in space and has been extensively studied elsewhere.[10-12]

is simply cloud albedo for normal incidence, assuming the integrated pulse energy is unity. This normalized escape GF can be thus treated as a probability density function (PDF) and we can proceed to compute its moments. An analogous GF can be defined for transmission where, by conservation at most lidar wavelengths, we have $T = 1-R$.

If detailed information about the space/time-dependent bi-directional properties of the cloud's radiative GFs is not available, then we make a standard Lambertian hypothesis:

$$G_R(t,x,y)dxdydt \approx \pi G_{obs}(t,\theta_\rho,\varphi)d_{obs}{}^2\sin\theta_\rho d\theta_\rho d\varphi dt. \tag{3}$$

The l.-h. side can be computed analytically in diffusion theory while the r.-h. side can be obtained from monostatically collected data (cf. Fig. 1). Using a numerical Monte Carlo (MC) model, Davis and Cahalan (1998) show that biases associated with the Lambertian assumption tend to cancel in the following spatial integrals, hence do not dominate the error budget.

The simplest in-cloud propagation characteristics of a laser pulse are: the mean photon pathlength,

$$\langle\lambda\rangle_R = c\langle t\rangle_R = c\iint dxdy\left[\int tG_R(t,x,y)dt\right] / R; \tag{4}$$

its 2nd-order moment (used, for instance, in pathlength variance $\langle\lambda^2\rangle_R - \langle\lambda\rangle_R{}^2$),

$$\langle\lambda^2\rangle_R = c^2\langle t^2\rangle_R = c^2\iint dxdy\left[\int t^2G_R(t,x,y)dt\right] / R; \tag{5}$$

and root-mean-square (rms) horizontal transport $\langle\rho^2\rangle_R{}^{1/2}$, where

$$\langle\rho^2\rangle_R = \int dt\left[\iint (x^2+y^2)G_R(t,x,y)dxdy\right] / R. \tag{6}$$

One can think of $\langle\rho^2\rangle_R{}^{1/2}$ as the gyration radius of the spot of diffuse light excited by the laser in cw mode. A major advantage of using the observables in Eqs. (4–6) is that there is no need for absolute calibration to estimate them from observations using Eqs. (1–3).

There are of course analogous quantities for transmission (subscript "T") that have been used in other studies: Veitel et al.[13] and Savigny et al.[14] for empirical results respectively in the temporal and spatial domains; Davis and Marshak[15] for the detailed theory that is, in large part, germane to reflection too.

2.2. Analytical results from diffusion theory

In absence of absorption, only two length scales are required to determine the optical properties of a plane-parallel medium in space/time as well as for constant/uniform illumination:

- the outer-scale H, and
- the inner-scale defined by the photon mean-free-path (MFP), $\ell = 1/\sigma = H/\tau$.

In the diffusion approximation, we are actually more interested in the "transport" MFP

$$\ell_t = \ell/(1-g) = 1/[(1-g)\sigma] \tag{7}$$

which, in essence, is the MFP for an effectively isotropic scattering; the rescaling by $(1-g)^{-1} \approx 6.7$ for $g = 0.85$ takes care of the propensity for forward (Mie) scattering by the cloud droplets.[16] One final parameter is introduced in diffusion theory to describe boundary conditions: the "extrapolation length" which we will denote $\chi\ell_t$. Here χ is an $O(1)$ numerical factor that can be used to minimize the approximation error although it is often set to 2/3, following Eddington's prescription,[17] or to $0.7104\cdots$ following asymptotic radiative transfer theory.[18]

A spatial-Fourier/temporal-Laplace solution of the non-stationary 3D diffusion equation by Davis et al.[10] with boundary/initial conditions describing a pulsed point-source leads to:

$$R = \frac{H}{2\chi\ell_t + H} = \frac{(1-g)\tau}{2\chi + (1-g)\tau} \tag{8}$$

for albedo in Eq. (2);

$$\langle\lambda\rangle_R = 2\chi H [\, 1 + C_{R\lambda}(1,\varepsilon) \,] \tag{9}$$

for mean pathlength in Eq. (4); and

$$\langle\lambda^2\rangle_R = \frac{4\chi}{5} H^2(1-g)\tau [\, 1 + C_{R\lambda}(2,\varepsilon) \,] \tag{10}$$

for the 2nd moment of pathlength in Eq. (5); and

$$\langle\rho^2\rangle_R = \frac{8\chi}{3} \frac{H^2}{(1-g)\tau} [\, 1 + C_{R\rho}(2,\varepsilon) \,] \tag{11}$$

for the variance in horizontal transport defined in Eq. (6). The radiative quantities in (9–11) contain pre-asymptotic correction terms given by:

$$C_{R\lambda}(1,\varepsilon) = C_{R\rho}(2,\varepsilon) = (\varepsilon/2)(1+3\varepsilon/2)/(1+\varepsilon), \tag{12a}$$

$$C_{R\lambda}(2,\varepsilon) = (\varepsilon/2)(8+41\varepsilon/2+75\varepsilon^2/4+\varepsilon^3/8)/(1+\varepsilon)^2; \tag{12b}$$

these corrections become small as

$$\varepsilon = 2\chi/(1-g)\tau = 2\chi\ell_t/H = T/R \tag{13}$$

decreases (τ increases).

We note that, apart from the precise proportionality constants dependent on χ, the leading terms in Eqs. (8–10) can be obtained from simple arguments based on the scaling/fractal properties of the random walks[19] executed by the lidar photons in the finite slab that defines the cloud. See Davis et al.[7] for R, $\langle\lambda\rangle_R$, and $\langle\rho^2\rangle_R$, and Davis[8] for $\langle\lambda^2\rangle_R$. For instance, the well-known fact that the order-of-scattering in reflected light goes as τ translates here to $\langle\lambda\rangle_R \propto H$, as can be seen in Eq. (9).

2.3. Comparison with Monte Carlo results

Going from bottom to top, Fig. 2 shows $T = 1-R$, $\langle\rho^2\rangle_R^{1/2}$, $\langle\lambda\rangle_R$, and $\langle\lambda^2\rangle_R^{1/2}$ from Eqs. (8–13) with $H = 1$ for simplicity and $\chi = 0.57$ to best reproduce the numerical results from straightforward MC simulations (symbols). Agreement is excellent

in the asymptotic regime, $(1-g)\tau \geq 10$, and reasonably good in the pre-asymptotic region, $1 < (1-g)\tau < 10$, with the correction terms in Eqs. (12–13).

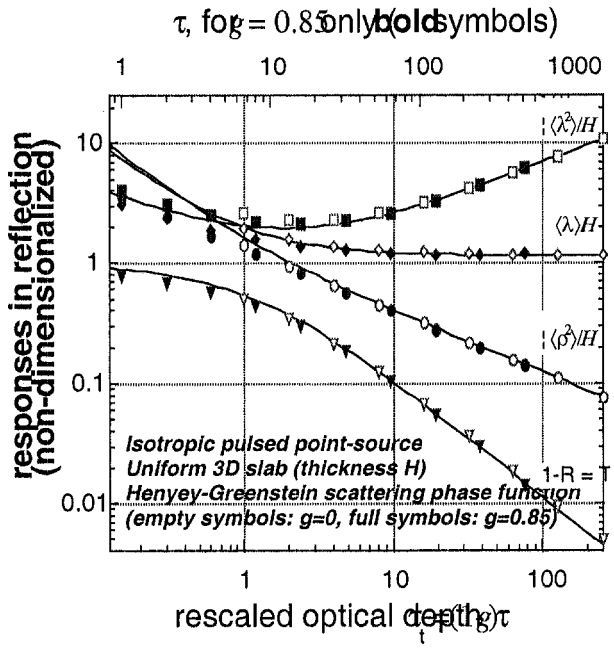

Figure 2: Analytical and Numerical Results for Off-Beam Cloud Lidar Observables. From bottom to top at right, we plotted $T = 1\text{-}R$, $\langle\rho^2\rangle_R^{1/2}/H$, $\langle\lambda\rangle_R/H$, and $\langle\lambda^2\rangle_R^{1/2}/H$, from Eqs. (8-13) with $\chi = 0.57$. Monte Carlo results are plotted for phase functions both isotropic and forward-scattering where a Henyey-Greenstein[20] model with $g = 0.85$ was used. We note the collapse of the numerical results, for the most part onto their analytical counterparts, when plotted against $(1-g)\tau = H/\ell_t$.

The MC computations were performed for a diffuse boundary-source rather than a normally incident collimated source that would better model a laser beam. Also, the phase function used in the simulations was Henyey and Greenstein's[20] rather smooth model rather than Mie calculations with a strong forward peak. However, these caveats only effects low orders-of-scattering which dominate the signal only if the clouds has a small optical depth; such clouds are readily probed by on-beam lidar methods anyway. Furthermore, the validity of the analytical theory can be extended to account for these directional effects by using the δ-Eddington reformulation of the diffusion approximation .[21]

2.4. Implications for off-beam lidar observations

From Eq. (11), the rms "spot-radius" $\langle\rho^2\rangle_R^{1/2}$ is found to be ≈0.3 km for the mean optical depth ($\tau \approx 13$) and physical thickness ($H \approx 0.3$ km) of marine stratocumulus (Sc), as observed by Cahalan and Snider,[22] and using the canonical $g = 0.85$ for warm clouds. This rms spot-size is a key quantity in the a priori signal-to-background ratio estimations by Davis and Cahalan.[23] Returning to the ground-based observation geometry in Fig. 1, $\langle\rho^2\rangle_R^{1/2} \approx 0.3$ km implies that we need a FOV of about 1 rad to capture about 2 rms distances if the cloud is at a range $d_{obs} \approx 1$ km. A couple of rms spot-radii, i.e., 0.5 km or so, is also the inherent resolution of a retrieval based on off-beam lidar observations, even if they are done continuously in time.

Optical depth τ is in fact highly variable at the sub-km scales of interest here: its range is from less than 5 to almost 100, hence $1^- \leq (1-g)\tau \leq 10^+$. This optical depth range alone leads to an albedo R between 0.9 and 0.3 in (8) which is another important factor in signal estimation. High R values imply that after the laser pulse hits cloud base plenty of light is eventually returned towards the ground.

The range of variation for H corresponding to that in τ is given partially by Pawlowska et al.'s[24] $\tau \propto H^{5/3}$ relation is 0.2–0.6 km. This relation applies however only to the adiabatic "cores" of Sc, hence to the relatively high τ values (>10) at the local maxima in the optical depth (or solar reflectance) fields; at the smaller but still highly variable τ's observed more frequently in sub-adiabatic regions, this τ–H coupling breaks down, with H varying spatially more slowly than τ in Sc.

For temporal quantities, we find $\langle\lambda\rangle_R$ to be somewhat larger than H, in the range 0.4–0.8 km, while the ratio $\langle\lambda^2\rangle_R{}^{1/2}/\langle\lambda\rangle_R$ falls between 1.5 and 2. These values were also used in the design phase of our instrument to set pulse-length requirements and time-binning strategies. Note that the precise choice for χ, always coupled to g and τ in our correction formulas (12a,b–13), has a minor effect on these λ statistics in the intermediate diffusive transport regime where correction terms are not negligible.

3. PROTOTYPE WIDE-ANGLE IMAGING LIDAR INSTRUMENT

We see from the above that, by combining the temporal and spatial information from off-beam lidar —the mean pathlength from the temporal Green function Eq. (9) and the mean-square horizontal displacement from the spatial Green function Eq. (11)— both the cloud thickness H and optical depth τ can be determined. While the primary spatial information lies in the radial displacement, the most informative realization of off-beam lidar would be one in which not only the radial and temporal distributions of the returning light are recorded, but its azimuthal dependence as well. This amounts to full time-resolved 2D imaging of the scattered radiation, in essence, a high-speed "movie" of the light propagation. With such a system, not only are quasi-uniform cloud fields amenable to azimuthally averaged analysis, but complex scattering mechanisms (scattering between clouds, etc.) in highly non-uniform clouds and broken cloud decks may also be observed and interpreted.

This is the approach we are taking at Los Alamos National Laboratory, and it relies on an imaging detector technology developed at LANL, the Micro-channel Plate/Crossed Delay Line (MCP/CDL) detector, coupled with high-speed pulse absolute timing electronics.[25] The MCP/CDL technology features photon-counting sensitivity, a large spatial format (4 cm diameter active area, effectively up to $\approx 1500^2$ pixels, and ultra-high time resolution (100 ps). It consists of the MCP/CDL detector — a photo-cathode coated vacuum tube, intensified by micro-channel plates, read out by a crossed delay line anode — together with fast pulse-timing electronics. Each photo-electron is intensified by a factor of 10^7, with positional information preserved, by the MCP. The electron cloud is collected by helically wound delay lines, producing in each line two counter-propagating current pulses which emerge from the ends. By measuring the arrival times of the pulses at the ends of the delay lines, the position of the original photon event is determined; with two orthogonal delay lines, both the x- and y-coordinates are determined.

This unique strategy for extracting spatial information distinguishes the MCP/CDL from other sensitive imagers such as gated/intensified CCDs in that it is intrinsically very fast, with photon arrival time automatically known to within 100 ps as a by-product of the imaging scheme. As an initial proof-of-principle test of the imaging lidar concept, we exploited this feature in laboratory-scale simulations of off-beam lidar observations where the "cloud" was a sizeable aquarium filled with a scattering liquid suspension.[26] Finally, we note that the focal-plane detector is not only capable of performing at very low light-levels, but actually requires them: too high a count rate ($>5\times10^6$/sec over the entire detector) confuses the timing-based imaging scheme.

These strengths and limitations drive the choice of laser for the imaging lidar system. The count rate limit demands a high repetition rate and averaging over many pulses. A repetition rate around 5–15 kHz is ideal, permitting maximal pulse averaging while avoiding the return from one pulse overlapping with the next. The MCP's spectral response makes a 532 nm frequency-doubled Nd:YAG laser a good choice. Our current laser produces 0.2 to 0.5 mJ/pulse, at a variable rep rate (12 kHz is typical in our experiments), with pulse widths ranging from 30 ns to 50 ns depending on operating conditions. The laser is triggered by a master clock, which also provides the timing reference for the detector system electronics.

Our current nighttime WAIL implementation uses a commercial medium-format SLR camera lens with a 35 mm focal length to feed the detector, thus obtaining the full-angle FOV of 60° prescribed in Section 2. One challenge in designing an imaging lidar system for clouds is the large dynamic range, several orders of magnitude, between the initial return (the traditional on-beam lidar signal) and the multiply scattered returns from locations at very large displacements from the beam. The faint large-displacement returns require a band-pass filter, $\approx$10 nm wide for nighttime work, to reject as much background light as possible. The use of interference filters presents an apparent problem, given the wide FOV, since, as is well known, the band center for standard interference filters varies strongly with angle of incidence. Over the 30° half-angle range of our system, the passband center wavelength shifts nearly 15 nm to shorter wavelengths as one moves from the center to the edge

of the field. This angular sensitivity, however, can be put to use to partially cancel the strong center-to-edge gradient intrinsic to cloud returns but challenging to any detector system, particularly to our MCP/CDL. If, instead of a filter centered (at normal incidence) at the laser wavelength, one chooses a somewhat longer nominal filter wavelength, light at large angles of incidence (i.e., coming from the edge of the FOV) will be near the angle-shifted center of the filter passband, while light near normal incidence (i.e., coming from the bright central spot) will be in the wings of the passband and be strongly attenuated. Figure 3 shows the empirical transmission function of our filter collection with respect to incidence angle out to 30° for 532 nm light.

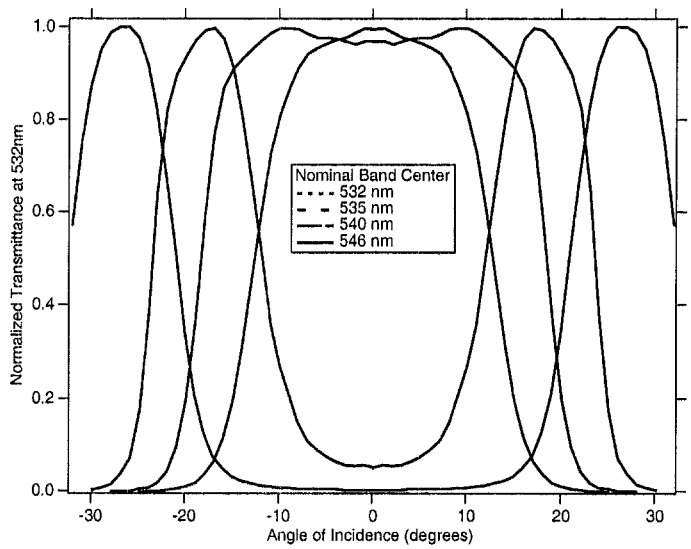

Figure 3. Bandpass Interference Filters as Angular Response Filters. Shown here are measured angular response curves for our selection of 10 nm bandpass interference filters at 532 nm. Used in front of an imaging lens, filters with normal-incidence band centers at wavelengths longer than 532 nm yield low transmission at the center of f.o.v., with an annular high transmission region at larger field angles.

4. WAIL OBSERVATIONS AND RESULTS

4.1. Sample dataset

In this example, we use WAIL data collected July 8, 1999, between 0:30 and 1:00 MST at LANL's Fenton Hill Observatory (35°52'45"N, 106°40'37"W). Figure 4 shows these nighttime results for a multi-layer cloud deck, probed with two different filters on the detector, one (nominal band center at 540 nm) which strongly suppresses the center spot, and the other (nominal band center at 536 nm) providing a more uniform response across the field. In each case, the spatially integrated return as a function of time is plotted, along with representative frames of the spatial WAIL "movie," each frame showing the full 60° FOV.

At early times, we see the near-field aerosol scattering. This eventually is followed by multiple cloud-base impacts and finally a strong spreading due to multiple scattering in the highest/densest layer. Due to the existence of a maximum allowable throughput for the focal-plane detector, the signal originating from the impact point and nearby is saturated, especially when the 532 nm (center-field) filter was used. However, we have minimized the impact of this loss of signal at small (in-cloud) pathlength λ and small horizontal displacement ρ by computing the space-time moments of interest further on using only the intermediate 540 nm filter. The effective truncation of long pathlengths and displacements compensates for the residual saturation at small times and angles. In an ideal situation, we would merge the signals from the more extreme (532 or 535 and 546 nm) filters in Figs. 4a–b before computing the moments in Eqs. (4–6). For QuickTime™ movie versions of these and other datasets, see http://nis-www.lanl.gov/~love/clouds.html.

4.2. Cloud property retrievals

In Fig. 5, the analysis of Section 2 is applied to the WAIL data presented in Fig. 4. Two methods for extracting physical cloud thickness H and optical depth τ are shown. The first uses only the temporal portion of the data, as might be obtained with non-imaging wide-angle lidar. The second technique uses both the space and time information from the imaging lidar data set, producing much smaller uncertainties in H and τ. The cloud parameters inferred from the two methods, however,

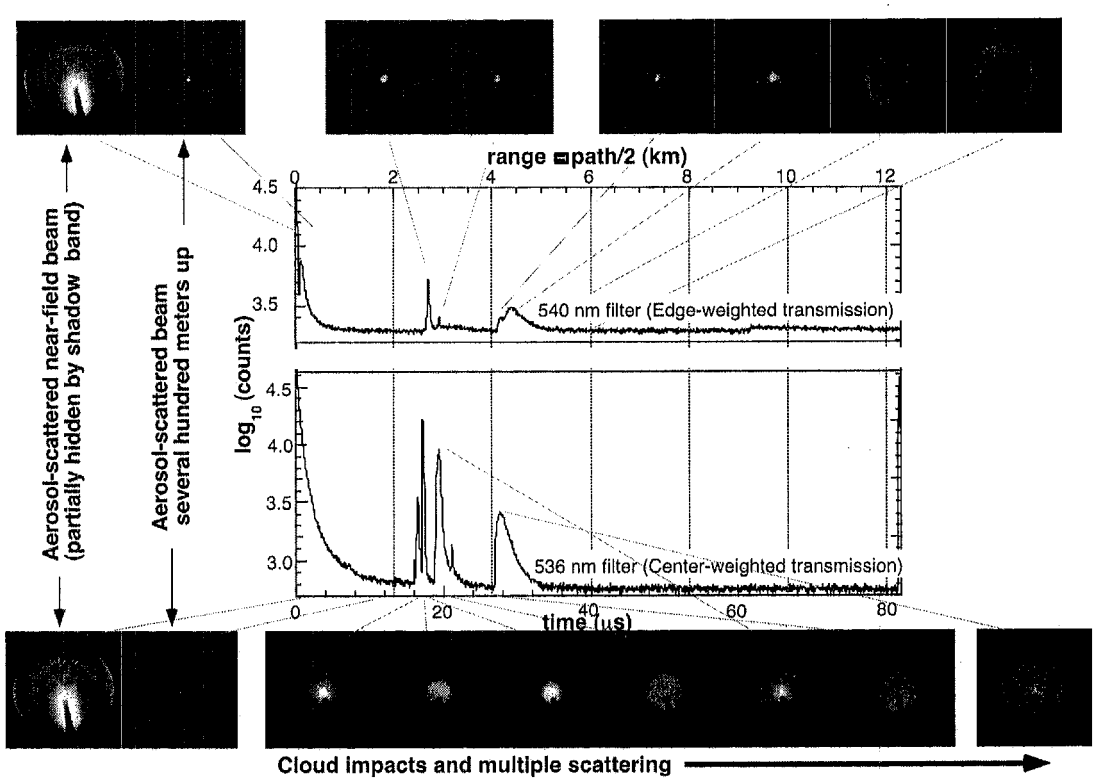

Figure 4: Nighttime WAIL Results. Shown here are the spatially integrated total return as a function of time (graphs) and a sequence of selected frames from the corresponding WAIL "movies" which show the spatial distribution of the returning light as a function of time. The full-angle FOV is approximately 60 degrees. Two data sets for essentially the same cloud deck are shown, being taken a few minutes apart. These were obtained with two different filters on the optics, one which emphasizes the large-angle returns (top) and the other emphasizing the center region (bottom). Narrow bandpass interference filters are generally used to reject background light, but also affect the spatial response of the system (see text and Fig. 3 for more details). Each sequence begins with the Rayleigh/aerosol-scattered beam as it leaves the laser (located off the bottom right side of the FOV); a shadowband blocks the brightest portion of this early return. For these early times, the system is effectively bistatic. Subsequent frames show the aerosol-scattered pulse several hundred meters up, the initial impact on the cloud deck, and subsequent spreading due to multiple scattering.

are consistent with each other and with climatology for the altostratus layer that was observed during that field trip. However, to achieve this congruence it is important to account for the internal stratification of the cloud layer. Indeed, we have plotted the results of numerical simulations similar to those described in §2.3 but with a collimated beam normally incident onto (1) uniform cloud models and (2) vertically stratified cloud models. Only the latter results explain the data in terms of the $\langle\lambda^2\rangle_R^{1/2}/\langle\lambda\rangle_R$ ratio used below. We assumed a linear increase of extinction from zero at cloud base to $2\tau/H$ at cloud top. This is a worst-case scenario since Brenguier's parameterization for adiabatic cores[27] calls for a linear increase in LWC which, in turn, leads to a 2/3 power-law in extinction.[9] The two versions of the 2-parameter retrieval procedure are as follows.

In both cases, the lower curve determines the optical depth τ. However, we immediately notice the large range of possible values for τ in Fig. 5a based on the ratio of ratios $\langle\lambda^2\rangle_R^{1/2}/\langle\lambda\rangle_R$ from (4–5) which yields 1.16: τ can be anywhere from 2 to 10 (even 1 to 20 or broader, given some measurement error). The cloud height information in Fig. 4 (this is an altostratus) argues for the lower end of the range in τ but we proceed without using this. From the upper curve, the cloud thickness can be determined, given the mean pathlength $\langle\lambda\rangle_R \approx 1.37$ km. The inferred value of H is, fortunately, not very sensitive to τ and we find H between 0.48 (possibly a little less, given some measurement error) to 0.56 km. This is reasonable for the nocturnal altostratus layer present in Fig. 4.

Substituting the response curves in Fig. 5b yields similar results, starting with $\langle\rho^2\rangle_R^{1/2}/\langle\lambda\rangle_R$ from (4) and (6) which yields 0.76, but there is less uncertainty in τ and H. The inferred value for τ of about 3 is quite reasonable for altostratus and the associated H is in middle of the previously obtained range, around 0.52 km. The time-only and space-time methods thus

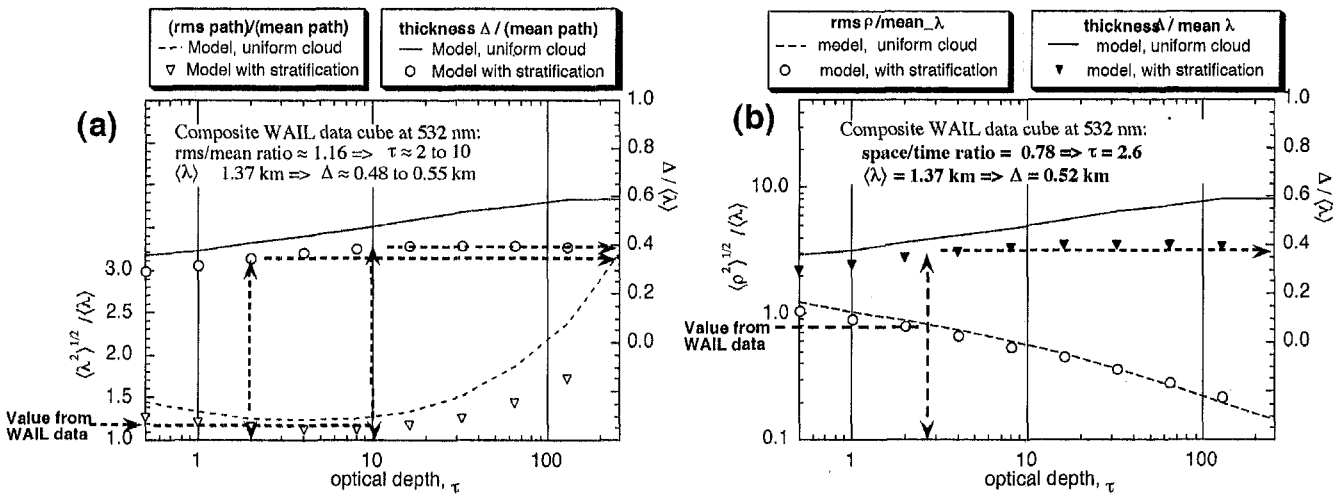

Figure 5: Retrieval of Cloud Properties from WAIL Data. (a) Time-only scheme. (b) Combined space-time scheme. The lower curves show calculated ratios of two different second-order moments to the first-order moment of the pathlength distribution. It is plotted vs. optical depth for a uniform cloud (line) and for a more realistic stratified cloud (symbols) in a ground-based geometry. The upper curves are calculated ratios of the cloud thickness to mean pathlength. Ratio values measured with WAIL (see main text) are indicated by the lower dashed horizontal line and , from there, vertical lines are drawn and optical depth is inferred; the mean pathlength was found to be ≈1.37 km, yielding physical cloud thickness (given the optical depth).

yield compatible results.

These results can now be used to infer the liquid water content of the cloud. Consider the well-known relation between optical depth and liquid water path (LWP), the vertical integral of LWC:[28] $\tau = (3/2)\mathrm{LWP}/\rho_W r_e$, where ρ_W is the density of liquid water (i.e., 10^6 g/m^3). Thus, with an additional assumption on the effective droplet radius r_e, the volume-averaged LWC can be estimated using an optical WAIL measurement alone:

$$\overline{\mathrm{LWC}} = \mathrm{LWP}/H = (2/3)\,\rho_W\,(r_e/H)\,\tau; \qquad (14)$$

no radiosondes, nor microwave instruments are required. For instance, taking $r_e \approx 10$ μm for simplicity, we find $\overline{\mathrm{LWC}} \approx 0.036$ g/m^3 in our altostratus case. Finally, the "natural" horizontal resolution we can assign to our (τ,H) estimates, and hence to $\overline{\mathrm{LWC}}$ in Eq. (14), is $\approx 2\langle\rho^2\rangle_R^{1/2}$. For our case-study, we obtain ≈1 km which is similar to those state-of-the-art meteorological satellites capable of synoptic coverage.

4.3 Detector Saturation and Improved Performance Using an Occulting Disk

The MCP/CDL detector has the advantages of high angular and temporal resolutions as well as extreme sensitivity, but has the disadvantage of a relatively low maximum allowable count rate, which necessitates co-adding many laser pulses in order to achieve good statistics on the scattered returns. The strong spatial gradient of the cloud returns, with most of the light coming from the nearly on-beam area, exacerbates this problem. We find that, even using the angular variation of interference filters flatten the dynamic range, as in Fig. 3 and Fig. 4, some residual saturation still occurs, and we have accounted for this in our analysis of the data.

To further reduce saturation effects, we have recently employed an occulting disk to completely mask the central region while obtaining large-angle data, thus providing complete suppression of the central high-intensity spot. The strategy here, as in the interference filter method, is to collect the central and wide-angle portions of the data set separately. First, using a fast f/#, wide-aperture lens setting, the wide-angle data is collected with the central region completely blocked. Then, with the lens stopped down and with additional neutral density filters as needed to prevent saturation of the central spot, an unsaturated central data set is collected with the occulting disk removed. We find that at the relatively high f/stops used, a

simple disk placed immediately in front of the filters provides full suppression of the central region, with a relatively fast transition to unobstructed transmission at larger field angles. Using this technique, we have obtained what appears in a preliminary analysis to be an essentially saturation-free data set, illustrated in Fig. 6; a detailed analysis is in progress at the time of this writing,

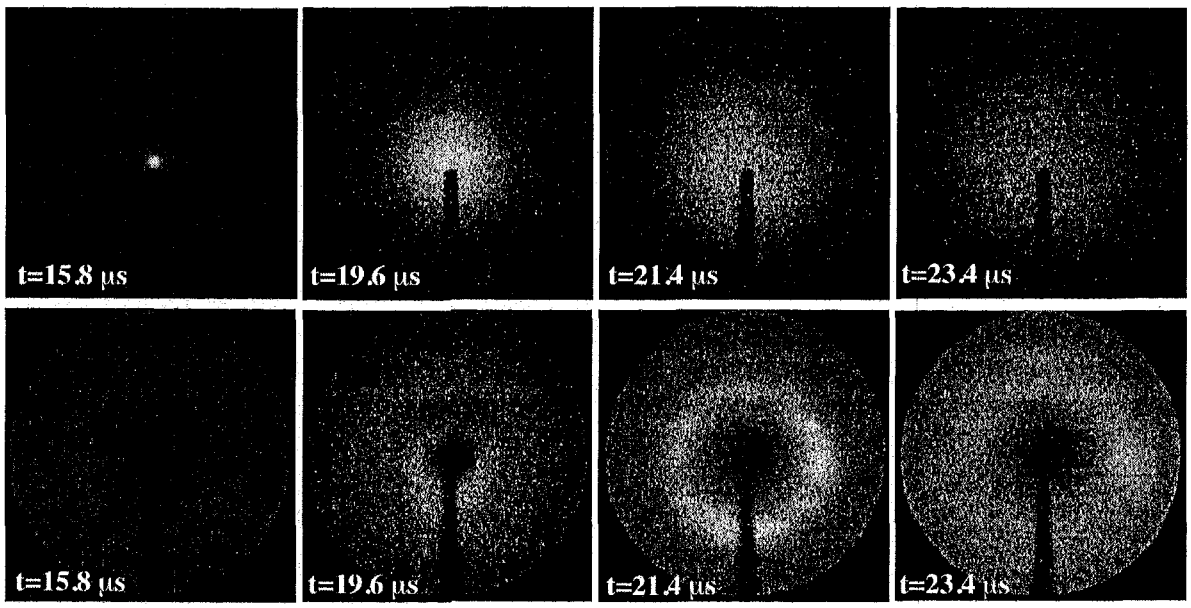

Figure 6: Use of an occulting disk to avoid central spot saturation. Shown here are representative frames from WAIL cloud scattering "movies" with the optics configured first (top row) to obtain the bright central region, then (bottom row) configured for the faint large-angle scattering. Combining the two data sets yields the full scattering Green functions. Optics configuration for the top row has the lens fully stopped down, plus an ND filter (effectively f/44), plus the "535nm" interference filter (see Fig. 3). For the bottom row, the lens is wide open (f/3.5) but with an occulting disk completely obscuring the central region, plus the "540nm" interference filter (see Fig. 3). Dark vertical band is a shadow band used to obscure the bright near-field laser beam in both cases.

5. SUMMARY AND OUTLOOK

We have shown that WAIL can be used to measure not only the distribution of multiply scattered photon pathlengths in a cloud, but also both the physical thickness of a stratiform cloud and its optical depth. It has been demonstrated elsewhere[8,29] that similar information can be extracted from a non-imaging spaceborne lidar system with a wide-enough FOV, e.g., the shuttle-based LITE mission. We used both the "time-only" method used for LITE data and a "space-time" method presented here in a case-study involving a moderately opaque altostratus layer (optical thickness around 3). Within instrumental and modeling error, both methods yield compatible results. However, the combined space-time scheme, which calls for a device with imaging (WAIL-type) or profiling capability, provides a much less ambiguous measure of optical depth. By obtaining both the vertical thickness and optical density, WAIL data can be used to infer cloud liquid water content.

For dense clouds that will extinguish on-beam backscatter lidar signals, an alternate technique exists to infer liquid water content in comparable detail: active microwave (mm-radar). These devices can provide a number of vertical bins, typically several per cloud layer, and with a horizontal resolution that depends on the observation strategy, but is typically a few hundred meters. So, at first glance, this complementary technology appears to yield more information than WAIL on cloud structure. However, Clothiaux et al.'s detailed comparisons[30] of mm-radar datastreams with counterparts from collocated (on-beam) lidar and other instruments underscore several problems in the conversion of radar reflectivities to the optical (shortwave) quantities required to pursue, say, climate studies. In contrast, off-beam lidar operates at wavelengths that are fully representative of solar radiative transfer. Assuming a tenuous enough cloud to still detect the usual on-beam lidar signal and sufficient skill to correct it for the multiple forward scattering, the inversion of this signal[31] is highly sensitive to the choice of backscatter ratio; this, in turn, depends on the phase function value for 180° scattering, which is a well-documented challenge to Mie theory. Being based on scattering through all possible angles, off-beam lidar does not have such sensitivities and the resulting spatial resolution is adequate for many applications.

There is a need for improved theory in off-beam lidar. In particular, the analytical approach grounded in photon diffusion theory can be extended at once to lesser optical depths and illumination by a collimated beam by using δ-rescaling of the optical properties in a 3D setting. Also, the numerical modeling can be enhanced by accounting for horizontal as well as vertical structure in the cloud. In this context, it is desirable to have codes to solve both the radiative transfer problem (using, e.g., Monte Carlo) and the diffusion problem (using, e.g., finite elements).

While WAIL provides a very exhaustive data set, extrapolation to a space-based system presents many technical challenges. Therefore, parallel to the WAIL project, collaborative work is currently underway at NASA Goddard Space Flight Center, focused on a scheme using more conventional detectors fed by fiber-optic bundles which route the light from pre-defined radial zones to several separate high-sensitivity photo-detectors.

Current work at LANL is focused on developing daylight capability for WAIL by means of ultra-narrow Faraday magneto-optic atomic line filters,[32-34] coincident with strong solar Fraunhofer absorption lines. With this strategy, which will use a dye laser transmitter tuned to the filter wavelength, we hope to be able to study the daytime clouds of direct interest to the solar scattering and absorption questions.

ACKNOWLEDGMENTS

This work was supported financially by the Laboratory Directed Research and Development (LDRD) program at LANL, under an "Exploratory Research" project. We thank A. Bird, D. Casperson and R. C. Smith for detector expertise and assistance with the data collection. We also thank R. Cahalan, A. Marshak, M. McGill, W. Priedhorsky, J. Spinhirne, J. Weinman, D. Winker, W. Wiscombe, and E. Zege for many fruitful discussions that helped shape this new approach to cloud lidar probing and its implementation in WAIL.

REFERENCES

1. R. D. Cess *et al.*, "Absorption of solar radiation by clouds: Observations versus models," *Science* **267**, 496–499 (1995).
2. P. Pilewskie, and F. P. Valero , "Direct Observations of Excess Solar Absorption by Clouds," *Science*, **267**, 1626–1629 (1995).
3. V. Ramanathan, *et al.*, "Warm pool heat budget and shortwave cloud forcing: A missing physics?," *Science* **267**, 499–503 (1995).
4. J. T. Kiehl, and K. E. Trenberth, "Earth's Annual Global Mean Energy Budget," *Bull. Amer. Meteor. Soc.*, **78**, 197 (1997).
5. K. Sassen, K., "Advances in polarization diversity lidar for cloud remote sensing," *Proc. IEEE*, **82**, 1907–1914 (1994).
6. L. R. Bissonnette, "Multipe scattering of narrow light beams in aerosols," *Appl. Phys. B*, **60**, 315–323 (1995).
7. A. B. Davis, D. M. Winker, A. Marshak, J. D. Spinhirne, R. F. Cahalan, S. P. Love, S. H. Melfi, and W. J. Wiscombe, "Retrieval of physical and optical cloud thicknesses from space-borne and wide-angle lidar," in *Advances in Atmospheric Remote Sensing with Lidar*, Eds. A. Ansmann, R. Neuber, P. Rairoux, and U. Wadinger, Springer-Verlag, pp. 193–196 (1997).
8. A. B. Davis, "Physical thickness and optical depth of stratocumulus from space-borne lidar, A moment-based diffusion method," *Technical Digest of OSA Topical Meeting on "Optical Remote Sensing of the Atmosphere"*, pp. 66–68, June 21–25, 1999, Santa Barbara (Ca), Optical Society of America, Washington, D.C. (1999).
9. J. Pelon, C. Flamant, V. Trouillet, and P. H. Flamant: "Optical and microphysical parameters of dense stratocumulus clouds during mission 206 of EUCREX'94 as retrieved from measurements with the airborne lidar LEANDRE 1,"*Atm. Res.*, **55**, 47–64 (2000).
10. A. B. Davis, R. F. Cahalan, J. D. Spinhirne, M. J. McGill, and S. P. Love, "Off-beam lidar: An emerging technique in cloud remote sensing based on radiative Green-function theory in the diffusion domain," *Phys. Chem. Earth (B)* **24**, 757–765 (1999).
11. S. D. Miller, and G. L. Stephens, "Multiple scattering effects in the lidar pulse stretching problem," *J. Geophys. Res*, **104**, 22205–22219 (1999).
12. D. M. Winkder, "Simulation and modeling of the multiple scattering effects observed in LITE data," in *Advances in Atmospheric Remote Sensing with Lidar*, Eds. A. Ansmann, R. Neuber, P. Rairoux, and U. Wadinger, Springer-Verlag, pp. 185–188 (1997).
13. H. O. Veitel, Funk, C. Kruz, U. Platt, and K. Pfeilsticker, "Geometrical pathlength probability density functions of the skylight transmitted by mid-latitude cloudy skies," *Geophys. Res. Lett.*, **25**, 3355–3358 (1998).

14. C. O. Savigny, Funk, U. Platt, and K. Pfeilsticker, "Radiative smoothing in zenith-scattered sky light transmitted through clouds to the ground," *Geophys. Res. Lett.*, 26, 2949-2952 (1999).
15. A. B. Davis , and A. Marshak: "Space-time characteristics of light transmitted by dense clouds," *J. Atmos. Sci.* (2001, submitted).
16. D. Deirmendjian, *Electromagnetic Scattering on Spherical Polydispersions*, Elsevier, New York (1969).
17. A. S. Eddington, "On the radiative equilibrium of stars," *Mon. Not. Roy. Ast. Soc.*, **77**, 16–35 (1916).
18. K. M. Case and P. F. Zweifel,: *Linear Transport Theory*, Addison–Wesley Publ. Co., Reading . Mass. (1967).
19. Mandelbrot, B. B., *The Fractal Geometry of Nature*, W. H. Freeman, San Fransisco (1982).
20. L. C. Henyey and J. L. Greenstein, "Diffuse radiation in the galaxy," *Astrophys. J.*, **93**, 70–83 (1941).
21. J. H. Joseph, W. J. Wiscombe, and J. A. Weinman, "The delta-Eddington approximation for radiative flux transfer," *J. Atmos. Sci.*, **33**, 2452–2459 (1976).
22. R. F. Cahalan and J. B. Snider, "Marine stratocumulus structure during FIRE," *Remote Sens. Environ.*, **28**, 95–107 (1989).
23. A. B. Davis, and R. F. Cahalan, "Off-beam (multiply-scattered) lidar returns from stratus, 1: Cloud-information content and sensitivity to noise," in *19th International Laser Radar Conference Proceedings*, Eds. U. Singh, S. Ismail, and G. Schwemmer, pp. 91–94, July 6–10 1998, Annapolis (Md), NASA Center for Aero-Space Information (CASI) (1998).
24. H. Pawlowska, J.–L. Brenguier, Y. Fouquart, W. Armbruster, S. Bakan, J. Descloitres, J. Fischer, C. Flamant, A. Failloux, J.–F. Gayet, S. Gosh, P. Jonas, F. Parol, J. Pelon, and L. Schüller, "Microphysical and radiative properties of stratocumulus clouds: the EUCREX mission 206 case study," *Atm. Res.*, **55**, 85–102 (2000).
25. W. C. Priedhorsky, R. C. Smith, and C. Ho, "Laser ranging and mapping with a photon-counting detector," *Appl. Opt.* **35**, 441–452 (1998).
26. A. B. Davis, C. Ho, and S. P. Love, "Off-Beam (Multiply-Scattered) Lidar Returns from Stratus, 2: Space-Time Measurements in a Laboratory Simulation," in *19th International Laser Radar Conference Proceedings*, Eds. U. Singh, S. Ismail, and G. Schwemmer, July 6–10, 1998, Annapolis (Md), NASA Center for Aero-Space Information (CASI) pp. 55–58 (1998).
27. J.–L. Brenguier, "Parameterization of the condensation process: A theoretical approach," *J. Atmos. Sci.*, **48**, 264–282 (1991).
28. G. L. Stephens, "Radiation profile in extended water clouds – Part 1, Theory," *J. Atmos. Sci.*, **35**, 2111–2122 (1978).
29. A. B. Davis, D. M. Winker, and M. A. Vaughan, "First Retrieval of Boundary-Layer Cloud Properties from Off-Beam/Multiple-Scattering Lidar Data Collected in Space" in *Laser Remote Sensing of the Atmosphere: Selected Papers from the 20th International Laser Radar Conference*, Eds. A. Dabas and J. Pelon, École Polytechnique, Palaiseau, France, (2001, in press).
30. E. E. Clothiaux, M. A. Miller, B. A. Albrecht, T. P. Ackerman, J. Verlinde, D. M. Babb, R. M. Peters, and W. J. Syrett, "An evaluation of a 94-GHz radar for remote sensing of cloud properties," *J. Atmos. and Oceanic Technol.*, **12**, 201–229 (1995).
31. J. D. Klett, "Stable analytical inversion solution for processing lidar returns," *Appl. Opt.*, **20**, 211–220 (1981).
32. G. Agnelli, A. Cacciani and M. Fofi, "The Magneto-Optical Filter," Solar Physics **44**, 509-518 (1975).
33. H. Chen, C. Y. She, P. Searcy, and E. Korevaar, "Sodium-vapor dispersive Faraday filter," Opt. Lett. **18**, 1019-1021 (1993).
34. B. Yin and T. M. Shay, "Theoretical model for a Faraday anomalous dispersion optical filter," Opt. Lett. **16**, 1617-1619 (1991).